Metered reagent injection into microfluidic continuous flow sampling for conductimetric ocean dissolved inorganic carbon sensing

OPEN ACCESS
IOP Publishing
Measurement Science and Technology
Meas. Sci. Technol. **31** (2020) 065104 (11pp)
https://doi.org/10.1088/1361-6501/ab7405

Metered reagent injection into microfluidic continuous flow sampling for conductimetric ocean dissolved inorganic carbon sensing

Mark Tweedie[1], Antonin Macquart[2], Joao Almeida[3], Brian Ward[3] and Paul Maguire[1]

[1] NIBEC, Ulster University, Belfast, Northern Ireland
[2] ams AG, Zurich, Switzerland
[3] AirSea Laboratory, Ryan Institute & School of Physics, National University of Ireland, Galway, Ireland

E-mail: m.tweedie@ulster.ac.uk

Received 1 November 2019, revised 13 December 2019
Accepted for publication 7 February 2020
Published 3 April 2020

Abstract

Continuous autonomous measurement of total dissolved inorganic carbon (TCO_2) in the oceans is critical for climate change modelling and ocean acidification measurement. A microfluidic conductivity-based approach will permit integration of miniaturised chemical analysis systems into Argo ocean floats, for long-term, high-accuracy depth profiling of dissolved CO_2 with minimal reagent payload. Precise metering, suitable for sample acidification and CO_2 liberation, is addressed. Laser etched microfluidic snake channel restrictors and asymmetric Y-meters were fabricated, with channel dimensions down to ~75 μm, to adjust metering ratios between seawater and acid simulants. Hydrodynamic resistances, from flow versus pressure measurements, were compared with finite element simulations for various cross-section profiles and areas. Microfluidic metering circuits were constructed from various resistance snake channels and Y-junction components. Sample to acid volume ratios (meter ratio) up to 100:1 have been achieved with 300 μm wide snake channels for lengths >m. At highest resolution, the footprint would be >600 mm^2. Circuits based solely on asymmetric Y-junctions gave maximum meter ratios of 16:1 with a footprint of <40 mm^2 and ~0.2% precision. Further refinement is required to ensure the integrity of such small channels in integration of metering units into full TCO_2 analysis microfluidic circuits.

Keywords: dissolved inorganic carbon, TCO_2, microfluidics, snake channel restrictors, hydrodynamic resistance, asymmetric Y-meters, meter ratios

(Some figures may appear in colour only in the online journal)

1. Introduction

Measurement of total dissolved CO_2 (TCO_2) content in seawater by miniaturised sensors in deep sea floats is set to become important for long term oceanic monitoring, as the oceans capture the increasing amounts of CO_2 released by fossil fuel burning [1]. Such measurements will feed into climate change modelling, to improve the accuracy of future global temperature rise predictions as monitored by the UN [2], and sea level rise prediction [3]. New microfluidic lab on chip devices for TCO_2 measurement must be developed for long-term autonomous deployment in a deep ocean environment. This poses severe challenges with regard to design, fabrication and testing. Oceanic studies of TCO_2 content in seawater have traditionally used sample collection by research vessels and

laboratory analysis. This is slow, expensive and has provided only sparse coverage, whereas continuous remote monitoring across the world's oceans and to depths of up to 3 km are required. Several methods have been demonstrated for field analysis of TCO_2, such as conductivity change [4–6], spectrophotometry [7–10], IR absorption analysis [11–14], gas chromatography [15], and membrane inlet mass spectroscopy [16–18]. Partial pressure of surface CO_2, pCO_2, has been measured from buoys, floats, and ships [19–21]. Microfluidics based conductivity and temperature sensors have been trialled in the ocean [22], with other devices also investigated for oceanic nitrate/nitrite and phosphate/phosphorus detection [23–26], ammonium ion measurement [27], manganese sensing [28] ocean acidification [29], biochemical and microbiology applications in similar extreme environments [30, 31].

The Argo network of ~5000 untethered autonomous ocean floats offers the possibility of continuous low cost TCO_2 measurements to the required spatial and depth resolution and therefore inspires the development of a suitable TCO_2 microfluidic platform which could meet the stringent constraints on size and power, as well as reliability in the harsh ocean environment. Argo floats are currently deployed to measure pressure, temperature and salinity using real time (instantaneous) sampling and measurement as they ascend to the surface from their target depth of 2–3 km [32]. The floats then transmit the data to satellite, then descending to a drift depth of 1500 m for 9 d, before the next descent to target depth. The 10 day cycle repeats continuously, with each untethered float having a projected lifetime of 3–5 years. TCO_2 measurements using laboratory prototypes or in short term ocean deployment have achieved the $\leq$0.2% precision thought to be necessary for ocean characterisation [5, 9, 10, 33]. However microfluidic implementations which meet volume, power, cost and reliability constraints struggle to reach the required accuracy. TCO_2 determination by conductivity measurement was originally proposed by Hall and Aller [4] and remains the approach with the greatest potential for low-cost and low-power miniaturisation compared to optical or mass spectrometry. However, with conductivity measurement, noise rejection is a much more demanding challenge.

Total dissolved CO_2 (TCO_2) in seawater exists mainly in the form of CO_3^{2-} (carbonate) and HCO_3^- (bicarbonate) ions, with small amounts of carbonic acid, and dissolved free CO_2 molecules. Acidification of seawater to reduce the pH (<4) converts the TCO_2 forms to aqueous CO_2 which can be separated from seawater by diffusing across a membrane into a receiving solution of NaOH. The CO_2 then reacts with NaOH to form CO_3^{2-} (pH $\geq$ 12) via the dominant reaction $CO_2 + 2OH^- \rightarrow CO_3^{2-} + H_2O$, figure 1 [4]. Under appropriate conditions, the replacement of OH^- with the lower mobility CO_3^{2-} ions provides a linear relationship between conductivity and TCO_2 concentration. A microfluidic TCO_2 analysis system would therefore consist of several integrated functional units to achieve (i) acid injection and mixing in seawater for pH reduction, (ii) membrane liquid—liquid exchange of aqueous CO_2 and (iii) conductivity measurement in a high concentration alkaline environment. The time taken for CO_2 membrane exchange via diffusion

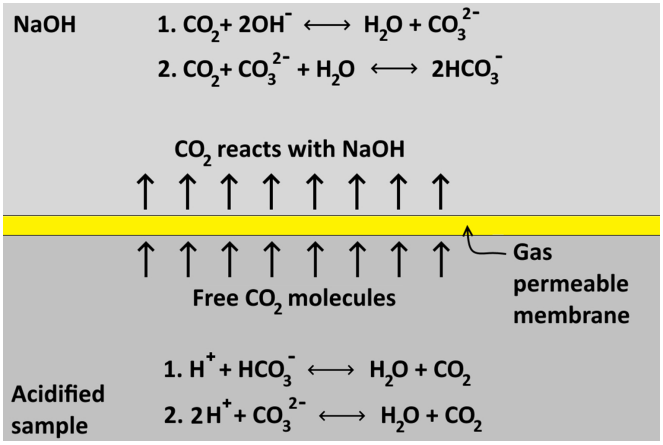

Figure 1. Gas diffusion from acidified sample into NaOH, for TCO_2 measurement.

prevents instantaneous measurement as the float ascends or descends and hence the only option is to collect seawater samples in microfluidic storage cells during ascent/descent for subsequent analysis while the float is parked at 1500 m for 9 d. Multi-sample membrane-based analysis poses new challenges for microfluidics fabrication including a requirement for high integrity multi-channel and multi-level structures with robust, long-term and chemically-resilient bonding. In recent work we have demonstrated suitable PMMA bonding processes for long term multi-layer and multi-channel operation [34], PDMS CO_2 membrane sealing within a PMMA manifold [35] and microfluidic CO_2 separation and conductivity measurement [36]. The requirement for sample storage plus the reagent (acid, NaOH) payload for measurement and flushing represents the primary contribution to system volume and maximum limits below ~1 l will be necessary. With P profiles (up to 150) per float life and N samples per profile (up to 100), reagent usage must ultimately be reduced to the microlitre per sample scale.

This work investigates one such unit, the injection of precise acid quantities into seawater. Reduction in seawater pH from its normal level (~8) to $\leq$4 is possible by adding a minimum quantity of high strength acid. To avoid the necessity of a separate acid pump which incurs a significant power and volume cost, simultaneous acid injection during the seawater sampling stage offers a possible solution. The controlled additional of acid is determined by the metering ratio (MR) of the microfluidic circuit where MR is the sample to acid volume ratio (V_S/V_A). The total acid payload volume is therefore $P \times N(V_S/\mathrm{MR})$ and maximising MR without incurring sample volume or other fabrication penalties is the objective. For a monoprotic acid, A, the maximum MR at which all TCO_2 is converted to CO_2 is $[A]/([TCO_2] + [CO_3^-])$, figure 1, which is ~300[A] for an upper $[TCO_2]$ limit in seawater of <3 mM and a carbonate fraction of ~10% at pH8. The addition of acid dilutes the sample and hence affects measurement precision, given by $P = (1 + \mathrm{MR})^{-1}$. To achieve a desired precision, P, the conditions to be met are

$$MR \geq \frac{1-P}{P}, [A] \geq \frac{[TCO_2]+[CO_3^-]}{P} \quad (1)$$

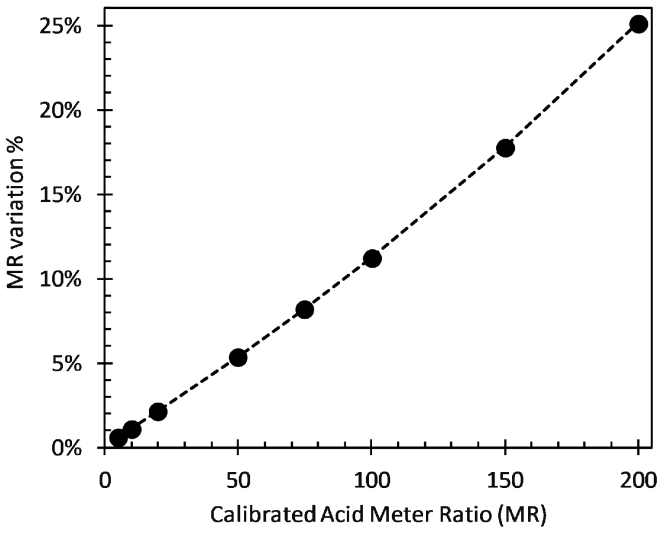

Figure 2. Effect of fluctuation in meter ratio (MR). The maximum allowed variation versus the calibrated MR to maintain precision $\leq$0.1%.

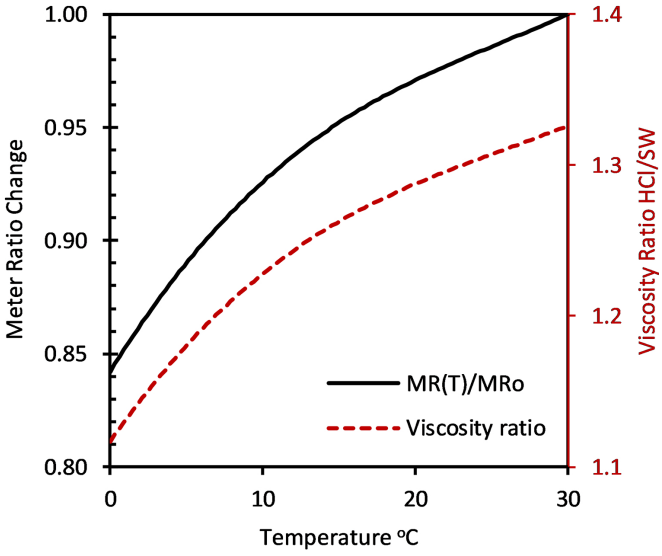

Figure 3. Calculated change in meter ratio (MR) and viscosity ratio of HCl (20%) and seawater, with salinity of 0.035 kg kg^{-1}. The calculations were based on equation (1), with a range of nominal MR values from 15 to 120. This represents the range of experimental MR values achievable using rectangular cross-section channels fabricated by precision milling.

A precision of 0.1% would require an acid concentration $[A] \geq$ 3M and MR ~ 1000 which is not realistic. The alternative therefore is to include the dilution factor within the device calibration. In this case the precision is now dependent on MR fluctuations during operation due to, for example, temperature and pump variability. The maximum allowed fluctuation in MR from the original calibrated value is shown in figure 2, for a specified precision of 0.1%. Since the resistance of acid and seawater channels depends on dynamic fluid viscosity, the MR temperature dependence needs to be considered over the likely ocean temperature variation from surface to 2 km depth. This variation is typically 10 °C but can reach up to 20 °C. The change in MR with temperature is calculated for two rectangular cross-section channels, figure 3, from the standard analytical approximation, (2):

$$R_H = \frac{12\mu L}{wh^3\left(1-\frac{h}{w}\left(\frac{192}{\pi^5}\sum_{n=1}^{\infty}\frac{1}{(2n-1)^5}\tanh\left(\frac{(2n-1)\pi w}{2h}\right)\right)\right)} \quad (2)$$

where R_{H} is the hydrodynamic resistance of a rectangular channel of length, L, width, w, and height, h, carrying a fluid of dynamic viscosity, μ. The nominal MR, given by $R_{\mathrm{H(acid)}}/R_{\mathrm{H(SW)}}$, is dependent on the ratio of acid (HCl) to seawater dynamic viscosity which reduces with depth, as the sea temperature falls, figure 3. For an expected temperature at depth of 5 °C and a maximum surface temperature of 25 °C, assuming 20% HCl concentration and an ocean salinity of 0.035 kg kg^{-1}, the change in MR is ~8%. To limit the effect of such a MR variation on TCO_2 measurement precision implies a minimum MR value of ~75, figure 2. With lower HCl concentration, the temperature dependence is attenuated. While it would be possible to factor the temperature dependence into the device calibration, this would require simultaneous temperature measurement at each depth sampling point.

In this paper we report the fabrication and characterisation of microfluidic structures suitable for single pump use in a continuous flow operation where metering is based on the channel resistance difference between two arms of a microfluidic junction. We implement various MR values via optimisation of channel cross-section area (CSA) or length. The latter involves uniform CSA which facilitates ease of fabrication at the expense of volume while the former involves differential CSA and presents a challenge for fabrication due factors such as channel height loss and deformation which are inevitable outcomes of thermoplastic bonding. Microfluidic performance has a strong dependence on the minimum achievable channel height and width values and their associated tolerances. While we have obtained sub-100 μm using precision milling, the need for long tightly spaced channels and variable heights and widths within a given pattern have proven to be problematic with this method. Instead we use laser etching to define channels, due to the pattern flexibility and higher resolution. However, laser etching, especially at the finest resolution, results in a loss of the traditional rectangular cross-section and hence the resultant channel resistance is no longer predictable. Along with pressure—flow and meter ratio measurements, we also report a number of finite element simulations with variable cross-section profiles used to estimate channel resistance.

2. Experimental

Microfluidic channels were engraved in cast PMMA (10 mm thickness) using a CO_2 laser, (Universal Laser Systems VLS2.30, 25 W source power, wavelength 10.6 μm), from AutoCAD patterns. A standard 1.5″ focal length lens was used for rastered snake channels, with lengths of 330, 663,

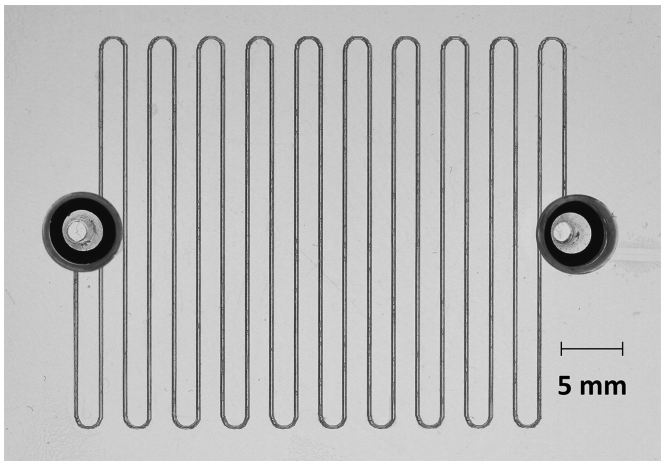

Figure 4. Snake channel, 663 mm length, with ¼-28 tapped ports.

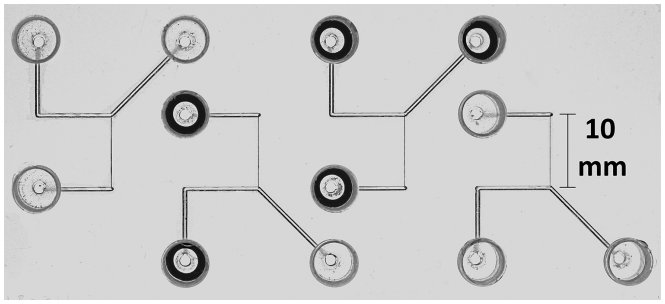

Figure 5. Asymmetric Y-meters, with ¼-28 tapped ports. Each Y meter has a different resistance in one input, via use of vector writing for narrower channels.

994 and 1320 mm, a typical example being shown in figure 4. The snake channels consisted of 30 mm straight sections with semi-circle turns at each end. All snake channels were rastered with settings of 100% power, 25% speed (~0.3 m s^{-1}), and AutoCAD drawing linewidth of 0.09 mm. A high power density focussing optics (HPDFO) lens was used for improved optical definition for fabrication of Y-meters, which required finer linewidths for narrow restrictions in a section of the acid input line. Fluidic connections were then attached via milled and tapped ¼-28 ports with 1 mm through holes. PMMA bonding was achieved via $CHCl_3$ solvent vapour treatment and subsequent thermal treatment (50 °C, ≥20 h), to drive off residual chloroform. Asymmetric Y-meters were fabricated with raster mode channels of nominal channel width 0.5 mm, except for a thin 10 mm long vector mode restrictive channel between the acid line input and the Y-junction. Laser vector mode operation gives a smoother line with straight edges in the Y direction. Four Y-meters with different restrictive channel cross-sections were fabricated, figure 5, with the Y-junction axis at 45° or 225° rotation.

A Dino-Eye AM7023 microscope eyepiece camera was used to acquire optical images of representative cross-sections of raster and vector-written channels in PMMA, as shown in figures 6 and 7, respectively. Image resolution, determined by the microscope objective lens of 5× or 10× magnification, was 0.51 µm/pixel, and 0.25 µm/pixel, respectively. The raster channels have a flatter base, because they are formed from

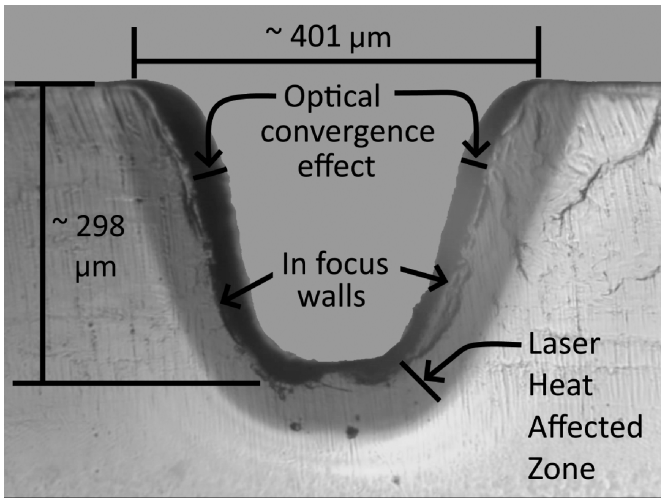

Figure 6. Rastered channel optical cross section, fabricated via a 1.5″ lens. The light shading below the in-focus channel walls is the laser heat affected zone (HAZ), typically seen where lasers eject molten material via application of thermal energy. The darker shading above the in-focus walls is an optical effect caused by parallax convergence, and falling illumination levels, when viewing along a long channel which progressively defocusses with distance.

at least two scan lines, while the vector channels are formed from one scan line, and so tend to V-shapes. Figure 6 shows in-focus channel walls, with shading both above and below the contour. The shading above is from the optical convergence effect when viewing down a long channel, while that below is from the laser heat affected zone, where the refractive index has changed due to the PMMA being partially melted there. The in-focus walls are sufficiently clear in figure 7 to allow the profile to be measured manually at multiple points, to within a few pixels. In practice, the laser channel width may vary by the order of a few 10's of µm, due to edge scalloping from the raster scan method, and focus variations due to thickness changes in the substrate.

The rastered example is shown without a bonded lid, while the vectored channels are shown after bonding to enclose them. Maximum channel width and height dimensions of the enclosed vector channels were obtained from image analysis (ImageJ), for a constant laser speed of ~0.3 ms^{-1}, figure 8. The cross-sectional area was determined using the ImageJ tracing function and area versus laser power is observed to be linear. Area values are most accurate with multi-point polygonal fitting, but a trapezium can also be adjusted to give an area approximation within a few % of the desired value, while staying close to the actual contours. However, a triangle fitted to the sides overestimates the area significantly, while one fitted to the vertices of the channel will greatly underestimate the area, so this shape is not suitable for modelling the real profile. Modelling of the Y-meters is not addressed here, however, this being limited to the snake channel restrictors instead. The rastered snake channel cross-sectional area was 7.35×10^{-8} m^2, which is >5× the largest vector area, and measured volumes ranged from ~18.5 µl to 73.5 µl.

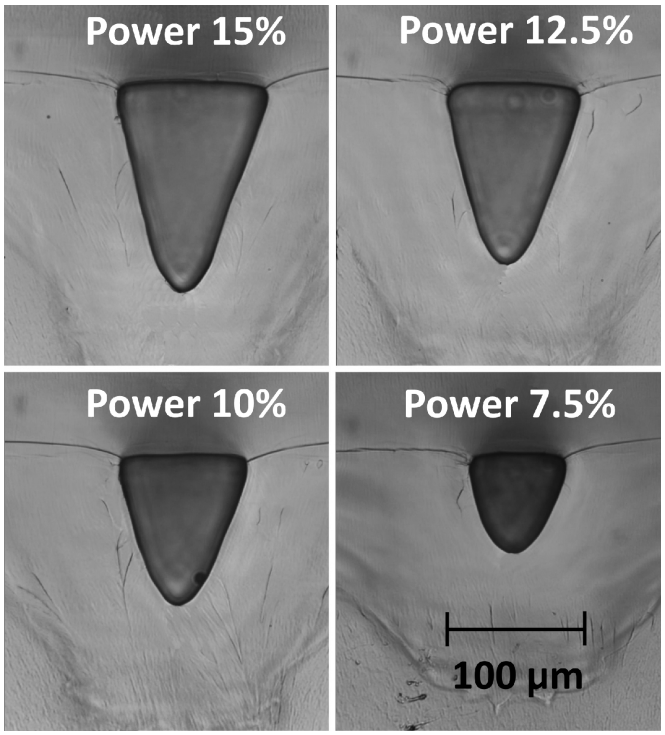

Figure 7. Vector written channel optical cross section (using HPDFO lens), post bonding, as a function of laser power (%). The maximum power is 25 W.

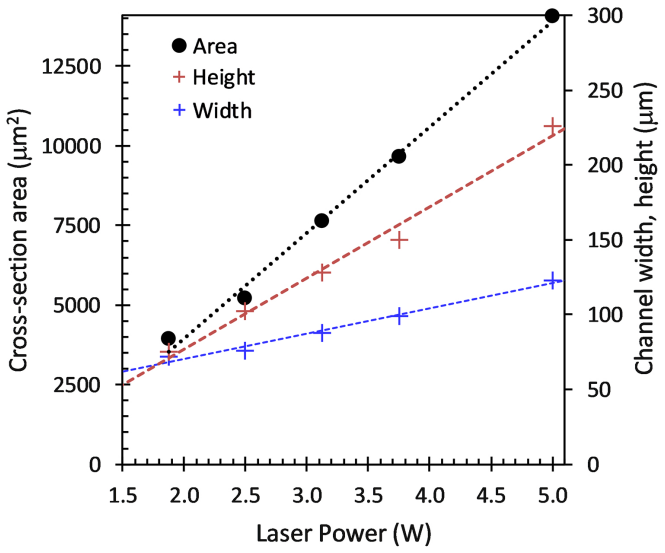

Figure 8. Dimensions of laser etched channels using vector mode with a HPDFO lens versus laser power, post bonding. Maximum channel width (W) and height (H) dimensions were obtained from calibrated microscopy images and cross-sectional area obtained from autotracing on images.

Metering ratios were determined using KCl standard solutions (Hanna Instruments) with high (1350–1550 µS cm^{-1}) and low (84–95 µS cm^{-1}) conductivity and DI water (1–2 µS cm^{-1}). Conductivity values were confirmed using a temperature-compensated Metrohm 712 probe meter. An

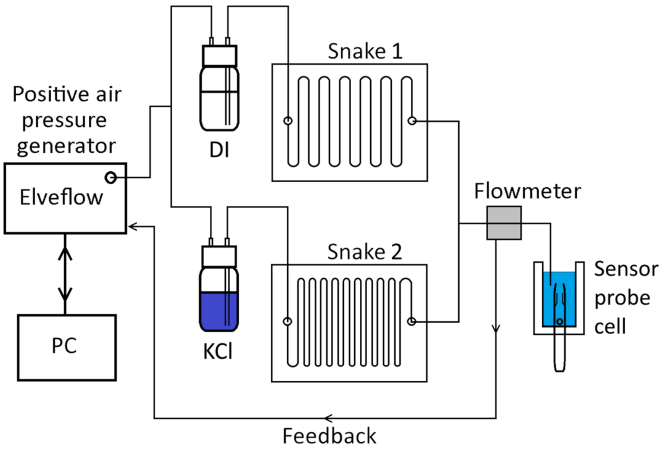

Figure 9. Elveflow positive pressure schematic for snake cell meter ratio testing, with flow sensor feedback (PC not shown).

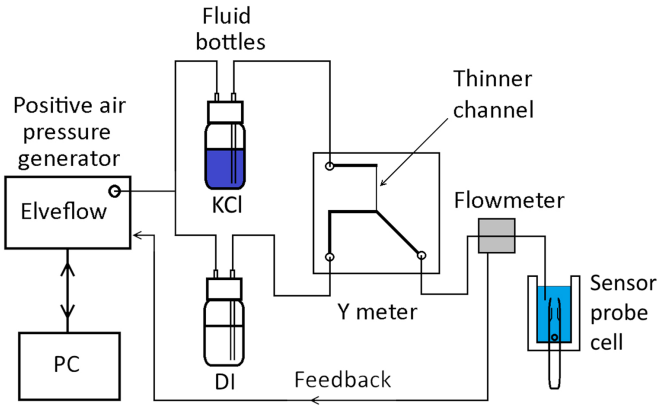

Figure 10. Elveflow positive pressure schematic with flow sensor feedback for Y meter measurements.

Elveflow AF1-P1600 pressure generator was used to drive fluid through microfluidic devices. Two experimental schematics are shown in figures 9 and 10, for snake channels and Y-meters, respectively. Elveflow flow meters with maximum rates of 1 ml min^{-1} and 5 ml min^{-1} under ESI software control were used to measure flow rates for known positive pressures and the hydrodynamic resistance, R_h, obtained from the inverse slope of flow rate versus pressure. For snake cells, high conductivity (~1500 µS cm^{-1}) and DI water solutions were simultaneously pumped using cells of different lengths positioned in each arm of the fluidic set up, figure 9. The outputs were combined at an equal T-piece, and the resultant conductivity measured in a 10 ml cell containing a temperature compensated 712 Metrohm conductometer probe.

The metering ratio is defined as the volume ratio of the two solutions (MR $= V_1/V_2$), where V_1 represents the seawater equivalent solution and V_2 represents the high conductivity acid solution. The final total volume is $V_T = V_1 + V_2$. By closing the V_2 channel, the value of V_1 can be determined. Alternatively, by assuming the same relationship between

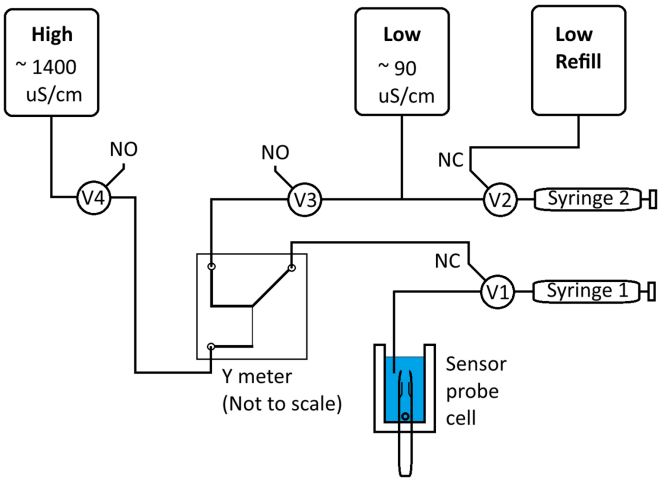

Figure 11. Cetoni NeMeSys syringe negative pressure schematic (PC not shown), for Y meter testing, with fluid in bags.

ion concentration and conductivity for all solutions, then $\sigma_T V_T = \sigma_1 V_1 + \sigma_2 V_2$ which can be rearranged to give

$$MR = \frac{V_1}{V_2} = \frac{\sigma_2 - \sigma_T}{\sigma_T - \sigma_1} \tag{3}$$

A similar set-up was used to measure the metering performance of three different Y-meters; see figure 10.

Tests were also performed under negative pressure, where the two fluids are simultaneously drawn through the devices, so representing the preferred configuration for an ocean deployed device for acid/seawater mixing. Cetoni NeMySys syringe pumps were used with precision glass-bodied Setonic syringes, as in figure 11. Here syringe 1 pulls fluid from both high and low conductivity solutions through the Y meter test device, and then dispenses 8 ml of the mixed solution into the conductometer probe cell. Aluminised DaklaPack 1 l spout-bags, specified as suitable for gasless liquids, were used to hold the fluids. The caps were fitted with Diba PTFE 2-way valves, and silicone applied to prevent fluid leakage. Syringe 2 in figure 11 takes fluid from the low refill bag and replenishes the low solution bag to its initial level, immediately after each mix sample is taken. Refill of the high solution bag is not necessary since the low:high mix ratios is >10:1.

3. Simulation

The theoretical hydrodynamic resistance, R_H, of a rectangular cross-section channel depends on width, w, and height, h, as in equation . For circular cross-section of radius R, it depends on R^{-4}. The high sensitivity of R_H to dimension and shape means that routine methods of estimating R_H for laser etched cross-sections are not available. Finite element modelling of fluid flow in channels of various cross-sectional shapes and dimensions was carried out using COMSOL Multiphysics software (v5.3). The COMSOL Mesh Settings were set for a Sequence type of Physics-controlled mesh. The mesh Element Size can be chosen from nine settings ranging from Extremely Fine to Extremely Coarse. The Coarse setting was used as, with

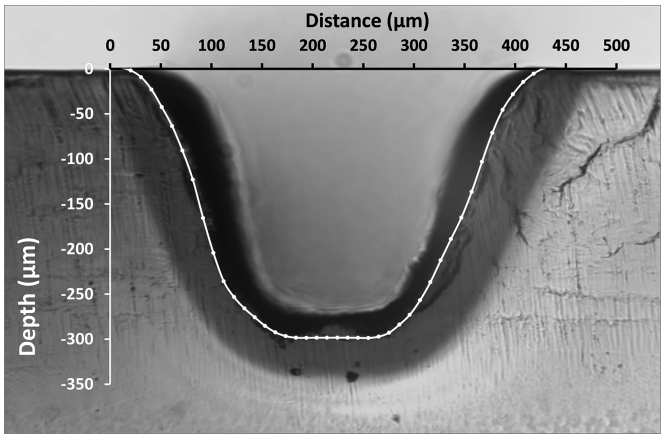

Figure 12. Outline of rastered channel, superimposed on original channel cross-section.

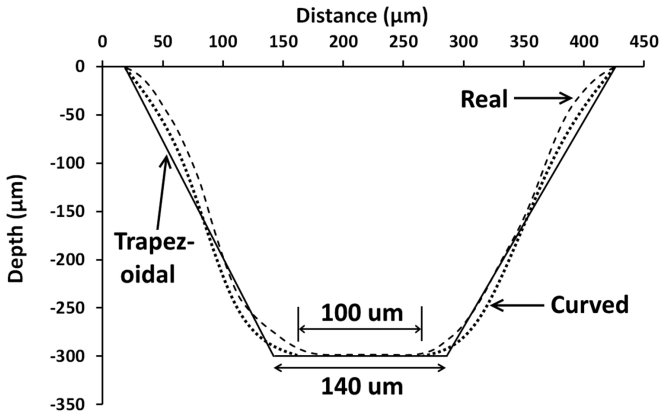

Figure 13. Approximate trapezoidal, curved and real wall profiles for rastered snake channel.

available computing power, simulations required about 2 h, this being taken to be an acceptable trade-off between precision and computational time. The boundary condition was set up for a wall condition of no slip, as typical for viscous fluids, on all channel surfaces.

Snake channel hydrodynamic resistance was determined by modelling one complete straight portion of 30 mm length, and 1 turn of diameter 2 mm, then multiplying the result by the number of turns. Channel cross-sections were modelled using a trapezoidal approximation with varying base widths, W_B, or using a curved profile obtained from a fit to the imaged cross sections. The rastered channel cross-section is shown in figure 12, with a base width of ~140 µm estimated from the flat region, and a comparison between trapezoid and smoothed fitted curve profiles is shown in figure 13. The maximum channel height and width are 401 µm and 298 µm respectively. From simulation, R_h increases as the base width of the trapezoid or fitted profile is reduced towards a triangular cross-section, with maximum of change of >200%; see figure 14. The resistance obtained from the fitted profile was up to 25% lower and less sensitive to base width. Resistances from both profiles are equal when the curved profile base width is ~40 µm less than that of the trapezoid; see figure 15.

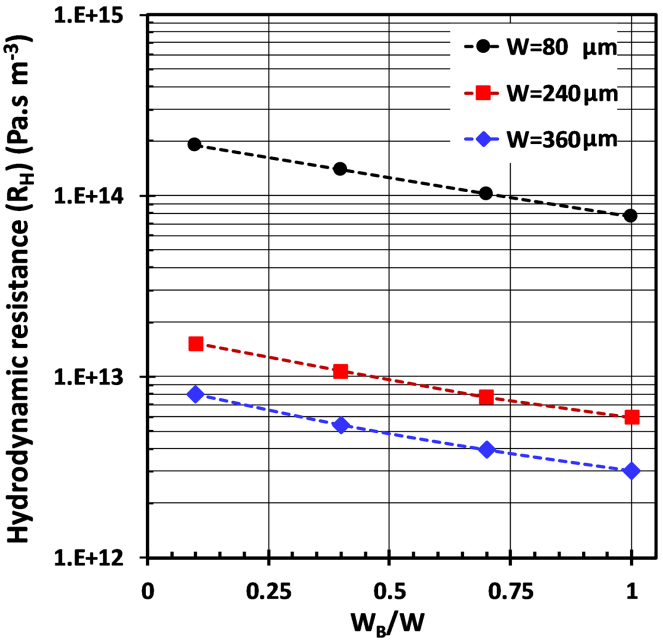

Figure 14. Impact on R_H of varying base width ratio (W_B/W) for top width values, W, from 80 µm to 360 µm. Simulation using fitted profile.

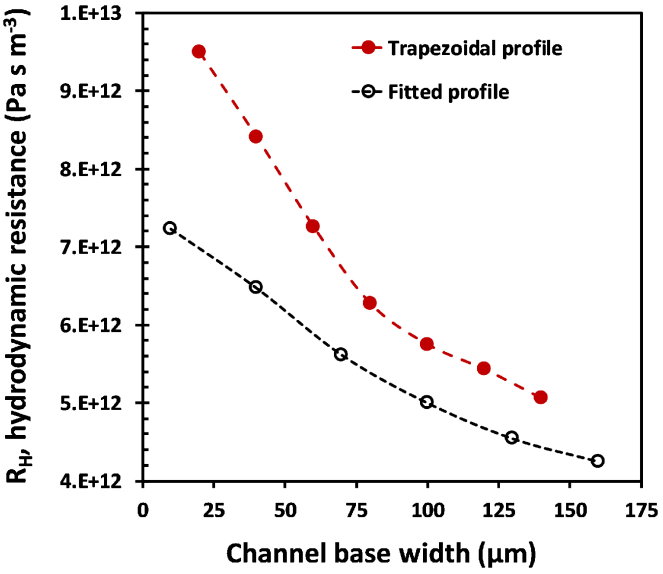

Figure 15. Simulated R_H versus base width for channels of curved and trapezoidal profiles with 390 µm and 298 µm width and height respectively.

4. Results and discussion

Graphs of flow rate versus differential pressure for each of the four snake channels were found to be linear for all devices, an example being shown in figure 16. The different flow rates are largely related to the four different channel lengths used. Consequently, the hydrodynamic resistance, R_H, which is obtained from the inverse gradient, and given in figure 17, shows, for constant cross-sectional area channels, R_H is proportional to snake channel length, as expected.

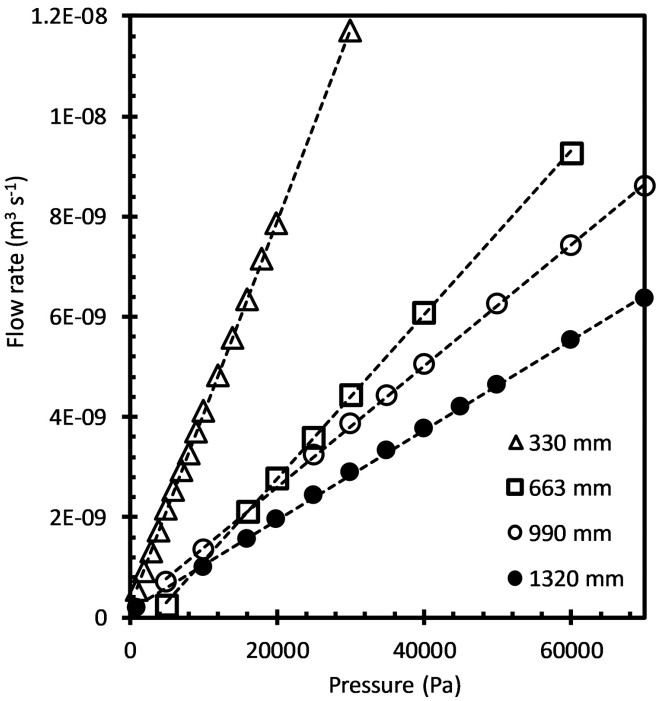

Figure 16. Flow versus pressure for snake channels of various lengths with dimension as in figure 12. Inverse gradients of fitted lines gives hydrodynamic resistance, R_H.

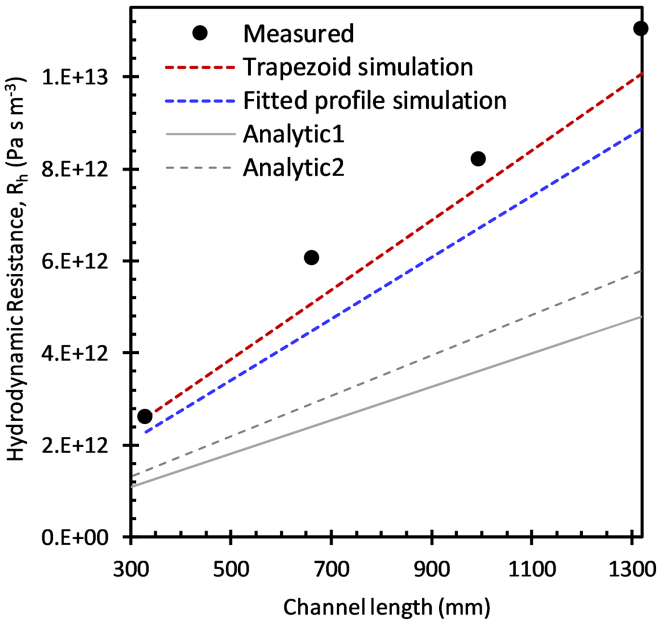

Figure 17. Measured hydrodynamic resistance, R_H, of snake channels versus length compared with simulated values using (i) trapezoidal and (ii) fitted curve cross-sections with a nominal base width of 140 µm and depth of 298 µm. Also shown are analytical calculations (equation (1)) for nominal (solid) and reduced heights (dashed).

The measured points do not lie in a perfectly straight line, however, because of fabrication errors. Firstly, there may be channel width and depth changes due to small laser focus errors arising from surface flatness deviations in the substrate.

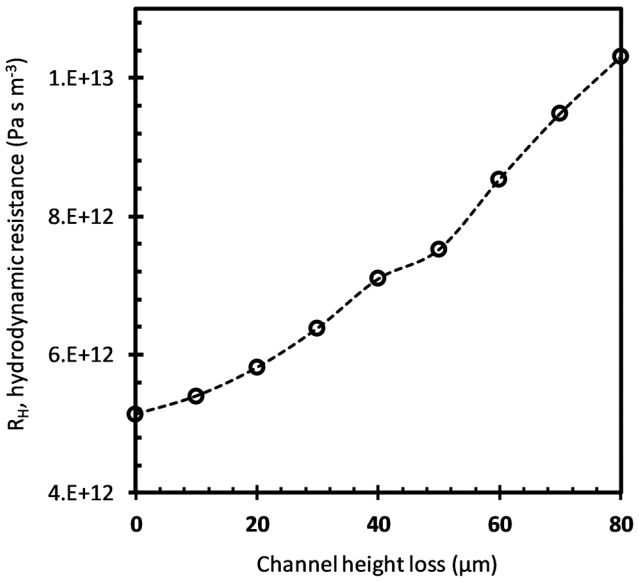

Figure 18. Simulated R_h versus reduction in channel height for a trapezoidal cross-section of 140 μm and a nominal height of 298 μm.

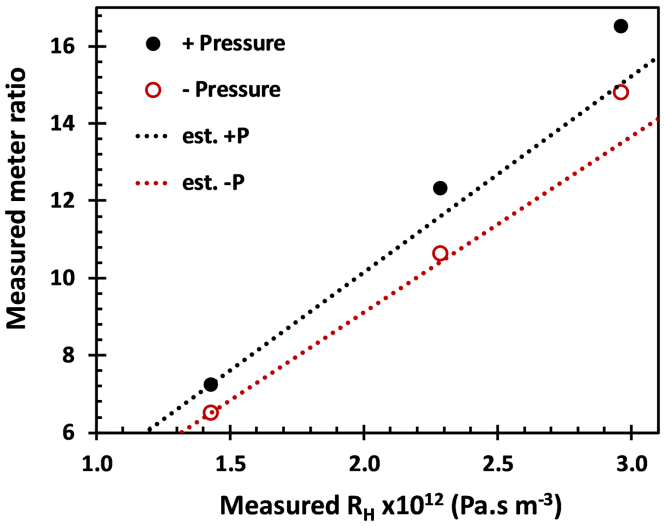

Figure 19. Single high resistance arm Y-meters: measured Y meter ratios under positive pressure (Elveflow) and negative pressure (Cetoni) flow against measured hydrodynamic resistance.

Table 1. Metering Ratios (MRs) for 1320 mm snake in high conductivity line, and shorter channels in low conductivity line, compared to MRs calculated from R_h measurements. MRs (from σ) use a value of 1510 μS cm^{-1} for the high-conductivity solution.

Low-conductivity channel length (mm)	330	663	994
Measured mixed solution conductivity, σ (μS cm^{-1})	285	543	658
MR (from σ)	4.29	1.78	1.29
MR (from R_h)	4.24	1.82	1.35
MR difference (%)	1.1%	−2.3%	−4.1%

Indeed, the focus setting itself has an error of about ±0.5 mm, since focus is set by aligning the lens head against a focus tool with a notch, and this is difficult to read to better than this accuracy. Fortunately, for general purpose use, the HPDFO lens focus tolerance is stated as ±0.7 mm, and the vertical *Z*-axis can be fine-tuned to 0.1 mm precision. To test focus tolerance, a focus error of 0.5 mm was measured to show a width change of ~15 μm on a 300 μm wide rastered channel (5% increase), and ~5 μm change on an ~80 μm wide vectored channel (6.25% increase). These channel width increases may be partly offset by the associated lower power density creating shallower features, so that the total cross-sectional area may not change by as great a percentage as the width. The laser head itself may, also, contribute a nominal ±1% variation due to power instability, although this is undetermined at present.

Other factors which can affect engraving performance are long build-up of debris on the laser lenses, and, short-term on the conical laser protective air flush nozzle. Occasionally, also, the air flush inlet water trap has to be drained of water, to prevent this being injected into the laser path and onto the workpiece, and significantly affecting the feature definition. So maintenance precautions have to be followed for best repeatability. Additionally, optical checks should be made on calibrated microscope images to confirm channel widths, and to measure depths via a focussing micrometer. Channel widths can also be confirmed using a stylus profilometer e.g. DekTak XT, and, if the stylus can reach the channel base, the depth can also be confirmed. Overall, with rigorous checks post fabrication, the channel consistency pre-bonding can be well controlled.

However, the greatest variable in device reproducibility is most likely to be the bonding of channels to a base. We have used $CHCl_3$ vapour assisted treatment of the base here for this purpose, and previously found from Raman studies that the $CHCl_3$ vapour penetrated to ~50 μm depth over ~10–12 min [34]. This layer is very soft, being saturated with $CHCl_3$, so that the way the two parts are brought together, with variable manual pressure applied, and the way pressure is applied and maintained thereafter during bond curing, can lead to significant variation in channel depth. Indeed, it is easily possible for channels less 100 μm width and depth to be accidentally blocked by polymer reflow at a single point, due to uneven application of pressure, and sideways movement of the parts after contacting. It is, of course, possible and advisable to check the channels after bond cure via an optical microscope to confirm channel widths, and depths via a focus micrometer, but this realistically, can only cover a few sample points. Ultimately, the measurement of flow rate versus pressure, and derived measurement of R_H, assists in confirming that the devices are performing satisfactorily.

Simulated values of R_H, using a trapezoidal cross-section with a base width of 140 μm and depth of 298 μm, as obtained from imaging, indicate a 15% reduction compared to the measured values and with a fitted curve cross-section, the simulated value is lower by a further ~10%. One possible reason for this discrepancy is the reduction of channel height and possible channel deformation observed after PMMA bonding where we have previously observed 15 μm–25 μm height loss after

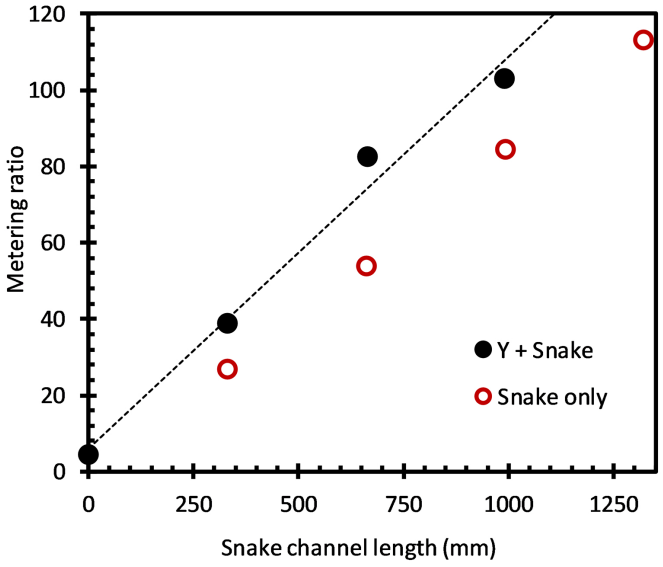

Figure 20. Meter ratios for single snake channel with asymmetrical microfluidic Y-junction circuit, in comparison with those for snake channel alone.

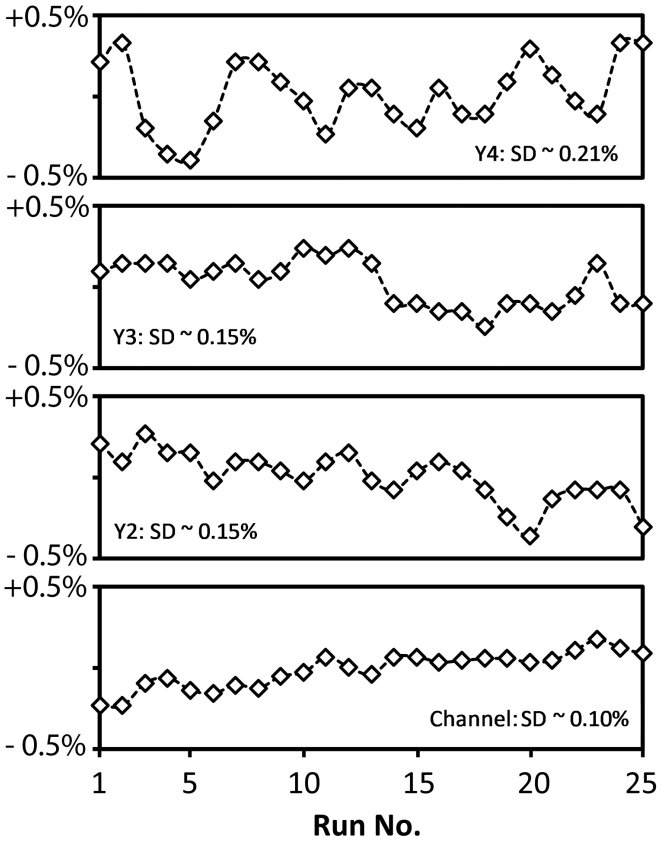

Figure 21. Relative conductivity variation for three different Y-meters, with high conductivity solution (1413 μS cm^{-1}) in high resistance line, and low conductivity solution (87 μS cm^{-1}) in low resistance line. Also shown is conductivity variation of channel only with direct dispense of KCl solution (84 μS cm^{-1}) without Y-meter.

$CHCl_3$ vapour assisted bonding [34]. The simulated impact of height loss on R_H is shown in figure 18, for the trapezoidal approximation, where the 15% resistance difference is equivalent to 23 μm height reduction. In achieving narrower channels for the high resistance acid line, we observe a change in profile from trapezoidal to almost triangular, with dimensions given in figure 8.

Metering ratios with snake channels in both high- and low-conductivity lines were determined from conductivity measurements and compared to those calculated from R_H measurements from the same devices. A 1320 mm snake was inserted in the high conductivity line (acid equivalent), while the low conductivity line was formed from each of the shorter snake channels in turn. The operational positive pressure was 60 mBar. Table 1 lists the measured meter ratios for each of the three versions, with a maximum of >4 for the shortest snake. Measured MR values and those predicted from R_H agree to within ~4%, illustrating that the meter ratios can be predicted with reasonable accuracy from the measured R_H values. These lower MR values may be used where the available valve technology is not specified for long term use with acid concentrations greater than ~0.1 M.

Meter ratios were also obtained from asymmetric Y-junction devices with one arm containing a short high resistance narrow channel obtained from vector mode laser etching, with dimensions as given in figure 8. Measurements were taken using both positive (Elveflow) and negative (Cetoni) pressure driven flow and MR values from 7 to 16 were achieved, in direct relationship to the measured channel resistance, figure 19. The small difference between positive and negative pressure measurements in likely due to the differences in external tubing length between both setups. Finally, the incorporation of an asymmetric Y-junction along with a single snake channel, of various lengths, was used to increase the MR above 100, figure 20. This illustrates the trade-off between area and MR. The area of the snake, at the highest pattern resolution, would be >600 mm^2 (6×10^{-4} m^2) while that of the Y-meter is <40 mm^2. The use of narrow/shallow vector mode channels, which have shown up to ×35 increase in resistance per unit length, would reduce the area requirement by up to a factor of 10. However, the integrity of long and shallow channels has yet to be demonstrated within the constraints of a full fabrication process, as illustrated here [34].

Meter ratio variability was determined for each of the Y-meter devices, given in figure 19. The rms precision values were found to be in the range 0.15%–0.21% while the solution conductivity/conductometer precision was ~0.10%, figure 21. These values are negligible with respect to impact on the overall TCO_2 measurement precision, figure 21.

5. Conclusion

Continuous and autonomous measurement of total dissolved inorganic carbon (TCO_2) in the oceans is critical for climate change studies, requiring miniaturised chemical analysis systems for ocean float-based deployment. A microfluidic conductivity-based approach offers the potential for such miniaturisation and sample pH reduction by acid injection to liberate dissolved CO_2 is required, which impacts on

total device payload. To address this, we have fabricated laser etched microfluidic snake channel restrictors and asymmetric Y-meters to adjust the metering ratio between sample and acid reagent. Laser etching conditions were varied to create a range of channel dimensions down to ~75 μm. Channel flow versus pressure measurements were used to determine hydrodynamic resistances which were compared with finite element simulations using a range of cross-section profiles and areas. Standard (laser raster mode) channels displayed specific R_H values of 8×10^{12} Pa.s m^{-3}, while narrow/shallower channels (laser vector mode) were 140–300 $\times$ 10^{12} Pa.s m^{-3}. Microfluidic metering circuits were constructed from variable resistance snake channels and dimensionally symmetric or asymmetric Y-junctions. Sample to acid volume ratios (meter ratio) up to 100:1 have been achieved with 300 μm wide snake channel for lengths >1 m. At the highest pattern resolution, this would require a footprint of >600 mm^2 (6×10^{-4} m^2). Circuits based solely on asymmetric Y-junctions gave meter ratios up to 16:1 with a footprint cost of <40 mm^2 and precision values of ~0.2%. Meter ratio variability was negligible with respect to overall TCO_2 analysis, compared to the impact of temperature via reagent and sample viscosity changes. Temperature dependence can be negated with the use of high MR ratios above 75. Further design and fabrication refinements will be required to ensure the structural and dimensional integrity of such small channels in future integration of metering units into full TCO_2 analysis microfluidic circuits.

Acknowledgments

The authors would like to acknowledge the funding support from: Invest N. Ireland (Grant No. RD0714186), The Department of Employment and Learning, N. Ireland (Grant No. US-IRL 013), Science Foundation Ireland (Grant No. 09/US/I1758), and National Science Foundation (US) (Grant No. NSF 0961250).

We would also like to acknowledge the support and advice of Todd Martz and Phil Bresnahan of Scripps Institute of Oceanography, UC San Diego.

ORCID iD

Mark Tweedie https://orcid.org/0000-0001-7073-0517

References

[1] Sabine C L *et al* 2004 The oceanic sink for anthropogenic CO_2 *Science* **305** 367–71
[2] IPCC 2016 *IPCC Fifth Assessment Report* Intergovernmental Panel on Climate Change
[3] Bamber J L and Aspinall W P 2013 An expert judgement assessment of future sea level rise from the ice sheets *Nat. Clim. Chang.* **3** 424–7
[4] Hall P J and Aller R C 1992 Rapid, small-volume, flow injection analysis for ΣCO_2, and NH4+ in marine and freshwaters *Limnol. Oceanogr.* **37** 1113–9
[5] Sayles F L and Eck C 2009 An autonomous instrument for time series analysis of TCO_2 from oceanographic moorings *Deep-Sea Res.* I **56** 1590–603
[6] Bresnahan P and Martz T 2018 Gas diffusion cell geometry for a microfluidic dissolved inorganic carbon analyzer *IEEE Sens. J.* **18** 6
[7] DeGrandpre M D, Hammar T R, Smith S P and Sayles F L 2003 In situ measurements of seawater pCO_2 *Limnol. Oceanogr.* **40** 969–75
[8] Nakano Y, Kimoto H, Watanabe S, Harada K and Watanabe Y W 2006 Simultaneous vertical measurements of in situ pH and CO_2 in the sea using spectrophotometric profilers *J. Oceanogr.* **62** 71–81
[9] Wang Z A, Chu S N and Hoering K A 2013 High-frequency spectrophotometric measurements of total dissolved inorganic carbon in seawater *Environ. Sci. Technol.* **47** 7840–7
[10] Wang Z A, Sonnichsen F N, Bradley A M, Hoering K A, Lanagan T M, Chu S N, Hammar T R and Camilli R 2015 In situ sensor technology for simultaneous spectrophotometric measurements of seawater total dissolved inorganic carbon and pH *Environ. Sci. Technol.* **49** 4441–9
[11] Kaltin S and Anderson L G 2005 Uptake of atmospheric carbon dioxide in arctic shelf seas: evaluation of the relative importance of processes that influence pco_2 in water transported over the bering-chukchi sea shelf *Mar. Chem.* **94** 67–79
[12] Fassbender A J, Sabine C L, Lawrence-Slavas N, De Carlo E H, Meinig C and Maenner Jones S 2015 Robust sensor for extended autonomous measurements of surface ocean dissolved inorganic carbon *Environ. Sci. Technol.* **49** 3628–35
[13] Bass A M, Bird M I, Morrison M J and Gordon J 2012 CADICA: continuous automated dissolved inorganic carbon analyzer with application to aquatic carbon cycle science *Limnol. Oceanogr. Methods* **10** 10–19
[14] Bass A M, Bird M I, Munksgaard N C and Wurster C M 2012 ISO-CADICA: isotopic—continuous, automated dissolved inorganic carbon analyser *Rapid Commun. Mass Spectrom.* **26** 639–44
[15] Hansen T, Gardeler B and Matthiessen B 2013 Technical note: precise quantitative measurements of total dissolved inorganic carbon from small amounts of seawater using a gas chromatographic system *Biogeosciences* **10** 6601–8
[16] Tortell P D 2005 Dissolved gas measurements in oceanic waters made by membrane inlet mass spectrometry *Limnol. Oceanogr. Methods* **3** 24–37
[17] Guéguen C and Tortell P D 2008 High resolution measurement of southern ocean co_2 and o_2/Ar by membrane inlet mass spectrometry *Mar. Chem.* **108** 184–94
[18] Bell R J, Short R T and Byrne R H 2011 In situ determination of total dissolved inorganic carbon by underwater membrane introduction mass spectrometry *Limnol. Oceanogr. Methods* **9** 164–75
[19] Friederich G E, Brewer P G, Herlien R and Chavez F P 1995 Measurement of sea surface partial pressure of C02 from a moored buoy *Deep-Sea Res.* I **42** 1175–86
[20] Fiedler B, Fietzek P, Vieira N, Silva P, Bittig H C and Kartzinger A 2013 In situ co_2 and o_2 measurements on a profiling float *J. Atmos. Oceanic Technol.* **30** 112–26
[21] Moore T S, DeGrandpre M D, Sabine C L, Hamme R C, Zappa C J, McGillis W R, Feely R A and Drennan W M 2011 Sea surface pCO_2 and O_2 in the Southern Ocean during the austral fall, 2008 *J. Geophys. Res.* **116** C00F11
[22] Huang X, Pascal R W, Chamberlain K, Banks C J, Mowlem M and Morgan H 2011 A miniature high precision conductivity and temperature sensor system for ocean monitoring *IEEE Sens. J.* **11** 12

[23] Beaton A D, Cardwell C L, Thomas R S, Sieben V J, Legiret F E, Waugh E M, Statham P J, Mowlem M C and Morgan H 2012 Lab-on-chip measurement of nitrate and nitrite for in situ analysis of natural waters *Environ. Sci. Technol.* **46** 9548–56

[24] Bowden M and Diamond D 2003 The determination of phosphorus in a microfluidic manifold demonstrating long-term reagent lifetime and chemical stability utilising a colorimetric method *Sens. Actuators B: Chemical* **90** 170–4

[25] Czugala M, Fay C, O'Connor N E, Corcoran B, Benito-Lopez F and Diamond D 2013 Portable integrated microfluidic analytical platform for the monitoring and detection of nitrite *Talanta* **116** 997–1004

[26] Legiret F, Sieben V J, Woodward E M S, Abi Kaed Bey S K, Mowlem M C, Connelly D P and Achterberg E P 2013 A high performance microfluidic analyser for phosphate measurements in marine waters using the vanadomolybdate method *Talanta* **116** 382–7

[27] Plant J N, Johnson K S, Needoba J A and Coletti L J 2009 NH4-Digiscan: an in situ and laboratory ammonium analyzer for estuarine, coastal, and shelf waters *Limnol. Oceanogr. Methods* **7** 144–56

[28] Provin C, Fukuba T, Okamura K and Fujii T 2013 An integrated microfluidic system for manganese anomaly detection based on chemiluminescence: description and practical use to discover hydrothermal plumes near the Okinawa trough *IEEE J. Oceanic Eng.* **38** 178–85

[29] Perez De Vargas Sansalvador I M, Fay C D, Cleary J, Nightingale A M, Mowlem M C and Diamond D 2016 Autonomous reagent-based microfluidic pH sensor platform *Sens. Actuators Chem.* **225** 369–76

[30] Fukuba T, Aoki Y, Fukuzawa N, Yamamoto T, Kyo M and Fujii T 2011 A microfluidic in situ analyzer for ATP quantification in ocean environments *Lab Chip* **11** 3508–15

[31] Fukuba T, Miyaji A, Okamoto T, Yamamoto T, Kaneda S and Fujii T 2011 Integrated in situ genetic analyzer for microbiology in extreme environments *RSC Adv.* **1** 1567–73

[32] Argo Argo—part of the integrated global observation strategy, Argo website (http://www.argo.ucsd.edu/)

[33] Liu X, Byrne R H, Adornato L, Yates K K, Kaltenbacher E, Ding X and Yang B 2013 In situ spectrophotometric measurement of dissolved inorganic carbon in seawater *Environ. Sci. Technol.* **47** 11106–14

[34] Sun D, Tweedie M, Gajula D R, Ward B and Maguire P D 2015 High strength thermoplastic bonding for multi-channel, multi-layer lab-on-chip devices for ocean and environmental applications *Microfluid. Nanofluid.* **19** 913–22

[35] Tweedie M, Sun D, Ward B and Maguire P D 2019 Long-term hydrolytically stable bond formation for future membrane-based deep ocean microfluidic chemical sensors *Lab Chip* **19** 1287

[36] Tweedie M, Sun D, Gajula D, Ward B and Maguire P D 2019 The analysis of dissolved inorganic carbon in liquid using a microfluidic conductivity sensor with membrane separation of CO_2 *ChemRxiv. Prepr.* (https://doi.org/10.26434/chemrxiv.8852087.v1)